Available online at www.sciencedirect.com
SCIENCE DIRECT®
International Journal of Heat and Mass Transfer 48 (2005) 703–718
International Journal of HEAT and MASS TRANSFER
www.elsevier.com/locate/ijhmt

Investigation of convective heat transfer augmentation using acoustic streaming generated by ultrasonic vibrations

Sinjae Hyun [a], Dong-Ryul Lee [b,*], Byoung-Gook Loh [c]

[a] *Biomedical Engineering Department, Mercer University, 30341-4155, USA*
[b] *School of Mechanical and Automotive Engineering, Catholic University of Daegu, 330 Keum Rak 1-ri, Hayang-Eup, Kyungsan, Kyungbuk, 712-702, Korea*
[c] *Department of Mechanical Systems Engineering, Hansung University, 136-792, Korea*

Received 5 August 2003; received in revised form 15 April 2004
Available online 21 November 2004

Abstract

An investigation of acoustic streaming induced by ultrasonic flexural vibrations is experimentally and numerically presented. The investigation includes acoustic streaming pattern, velocity, and associated heat transfer characteristics. Acoustic streaming patterns visualized using Acetone agree well with the prediction by Nyborg's theory. Tests of streaming velocity utilizing Styrofoam showed that the acoustic streaming velocity measured prove to be two orders greater than that by Nyborg's theory. CFD simulations also showed the same order of the velocity as the one measured. By virtue of acoustic streaming, a notable temperature drop of 40 °C was obtained in 4 min and maintained. Tests identifying major heat flow paths indicated that gaps and the vibrating beam serve as major heat flow paths.

CFD simulations were conducted to observe acoustic streaming patterns and velocities in the gap. Simulation results were validated by performing heat transfer analysis based on a lump-energy method. Simulation predicted that two symmetric vortices within half wavelength, rise of air at anti-nodes, and descent at nodes as Nyborg's theory predicts. The presence of the upper plate has no effect on the acoustic streaming patterns. However, when an upper plate shorter than the vibrating plate is used, a drastic increase in streaming velocity occurs at the edges of the upper plate due to entrainment of air, which also alters streaming pattern in the vicinity of the open end. Estimated streaming velocities from CFD simulations are found to be two orders greater than those based on Nyborg's theory.

The results of CFD simulation indicated the vortical flows induced by a ultrasonic flexural standing wave (UFSW) can be reproduced. The CFD results are experimentally validated, qualitatively through flow pattern comparisons and quantitatively by the transient temperature drop comparison. The CFD results showed that the velocity near the plates is of the order of 10–100 cm/s, which is over 100 times higher than the results from theoretical studies based on sonically induced acoustic streaming assuming inviscid flow.

Keywords: Heat transfer augmentation; Acoustic streaming; Ultrasonic flexural vibration; Resonance; Secondary airflow; Forced convection heat transfer

* Corresponding author. Tel.: +82 53 850 2717; fax: +82 53 850 2710.
E-mail address: dlee@cu.ac.kr (D.-R. Lee).

0017-9310/$ - see front matter © 2004 Elsevier Ltd. All rights reserved.
doi:10.1016/j.ijheatmasstransfer.2004.07.048

1. Introduction

Acoustic streaming is to show a tendency for a steady circulation to occur near the surfaces of obstacles and vibrating elements, and near bounding walls in a high-intensity sound field. It is spatial attenuation of a wave in free space and the friction between a medium and a vibrating object (cf. [1]) that have been known to induce acoustic streaming. When sound waves propagate they are lessened by absorption and scattering. This decrease is in general insignificant in a short distance of propagation. However, the propagation of a high intensity sound wave causes the decrease of pressure important enough to produce a steady bulk airflow. This type of streaming is usually associated with high-viscosity materials. The other type of acoustic streaming is ascribable to the friction between a medium and a solid wall when the former is vibrating in contact with the latter or vice versa (cf. [2]). It is not of significance whether the source of a relative motion results from either acoustic oscillations in the fluid or vibrations of the solid as long as there is an oscillating tangential relative velocity. Both cases lead to shear dissipation within Stokes boundary layer. Unlike acoustic streaming arising from spatial attenuation, this streaming has two cases; inner and outer streaming. The inner streaming is induced within the boundary layer due to the friction between the medium and the wall. Then, the inner streaming also creates relatively large scale steady streaming outside the boundary layer. It is reported that the acoustic streaming is especially effective in improving certain kinds of rate of transport process occurring on the fluid and solid interface including heat transfer, electrical effects, changes in biological cells, and removal of loosely adhering surface layers.

Faraday [3] found currents of air to rise at displacement anti-nodes on plates, and to descend at the displacement nodes. The first theoretical analysis of acoustic streaming phenomenon was accomplished by Rayleigh [4]. More investigation of the theory was performed by Schlichting [5], Nyborg [2], and Lighthill [6] where emphasis was laid on the fundamental role of dissipation of the acoustic energy in the change of the gradients in the momentum flux. In the research of Jackson and Nyborg [7], acoustic streaming induced by sonic longitudinal vibration is investigated. Acoustic streaming induced by ultrasonic flexural traveling waves is studied for a micro-electric and mechanical applications and negligible heat transfer capability of acoustic streaming is reported (cf. [8]). Gould [9] studied heat transfer across a solid–liquid interface in the presence of sonically induced acoustic streaming. Gopinath and Mills [10,11] investigated convective heat transfer due to acoustic streaming across the ends of a Kundt Tube. Selected references gives an overview of the works done for studying the heat transfer characteristics of acoustic streaming (cf. [12–14]).

Most of previous researches focused on acoustic streaming induced by sonic longitudinal vibration in an enclosed channel such as Kundt tube. Not much research on acoustic streaming induced in an open space by ultrasonic flexural vibration has been accomplished so far. Ultrasonic vibration significantly promotes acoustic streaming velocity. As a result, corresponding convective heat transfer rate can grow to the extent that conventional fan-based cooling device can supply. In addition, ultrasonic vibration offers silent operation. Utilizing flexural vibrations as a source of acoustic streaming allows for slim profile and low power operation because flexural impedance of an elastic beam is generally much smaller than longitudinal impedance. These advantages make ultrasonically induced acoustic streaming an alternative to conventional convective cooling using a motor-driven fan. To take full advantage of this promising technology, it is necessary to understand the nature of formation of acoustic streaming, its transient characteristics, streaming velocity, and associated convective heat transfer augmentation.

Therefore, the objective of this research is to experimentally and numerically investigate the steady characteristics of momentum and heat transfer owing to outer acoustic streaming induced by ultrasonic flexural vibrations in an open channel. Primary focus is placed on experimental observations of the cooling phenomenon, numerical simulations employing computational fluid dynamics (CFD), and their comparison with the present analytical heat transfer solutions.

2. Theoretical background

Nyborg [2] formulated the equation for near boundary acoustic streaming using successive approximation method as

$$\mu\nabla^2 u_2 - \nabla P_2 + F = 0 \tag{1}$$

$$F \equiv -\rho_0\langle(u_1\cdot\nabla)u_1 + u_1(\nabla\cdot u_1)\rangle \tag{2}$$

where μ is dynamic viscosity, ρ_0 is constant equilibrium density, u_1 is oscillatory particle velocity, u_2 is acoustic streaming velocity, P_2 is a steady state "dc" pressure, F is nonlinear driving forcing term, and $\langle\rangle$ means a time average over a large number of cycles. Without averaging, F contains a dc part and harmonically varying terms. The former induces acoustic streaming. When averaged over a long period of time, the effect of harmonically varying forcing terms disappears and only the contributions from the dc part appear in the solution. The acoustic streaming velocity, u_2 approaches a constant value as the distance from the vibrating beam approaches infinity. This time-independent limiting velocity, U_L is given by

$$-\frac{3}{4\omega}U_0\left(\frac{\mathrm{d}U_0}{\mathrm{d}x}\right) \tag{3}$$

where ω is excitation frequency, U_0 is amplitude of irrotational velocity tangent to the boundary (cf. [15]). To calculate outer acoustic streaming motion, the limiting velocity, U_L is used as a slip velocity at the solid surface by assuming Stoke boundary layer thickness negligible (cf. [6]). The right-upper wave pattern of Fig. 1 shows a theoretical acoustic streaming pattern induced by a flexural vibration defined as $A\sin(2\pi x/\lambda)\sin\omega t$ where A is the peak vibration amplitude and λ is the wave length. It is noted that separate circular airflow patterns near the vibrating beam and the stationary beam are present. Their relative size and rotation direction is determined by the limiting velocity in Eq. (3). Using linear acoustic theory and applying boundary conditions of $\mathrm{d}y/\mathrm{d}t = A\omega\sin(2\pi x/\lambda)\cos\omega t$ at $y = 0$ and $\mathrm{d}y/\mathrm{d}t = 0$ at $y = h$, U_0 is obtained as $-A\omega K_b\cos K_y(h-y)\cos(K_b x)/\{K_y\sin(K_y h)\}$ where $K_b = 2\pi/\lambda$, $K_y = \sqrt{K^2 - K_b^2}$, and K is acoustic wave number defined as ω/C where C is speed of sound. Therefore, the irrotational velocity at the vibrating beam, U_{0v} is given by $A_v\cos(K_b x)$ where $A_v = -A\omega K_b\cos(K_y h)/\{K_y\sin(K_y h)\}$. Similarly, the irrotational velocity at the stationary beam, U_{0s} is given by $A_s\cos(K_b x)$ where $A_s = -A\omega K_b/\{K_y\sin(K_y h)\}$. Substituting the irrotational velocity into Eq. (3) gives the limiting velocity. The limiting velocity is given by

$$\frac{3A_L^2\sin 2K_b x}{8C} \tag{4}$$

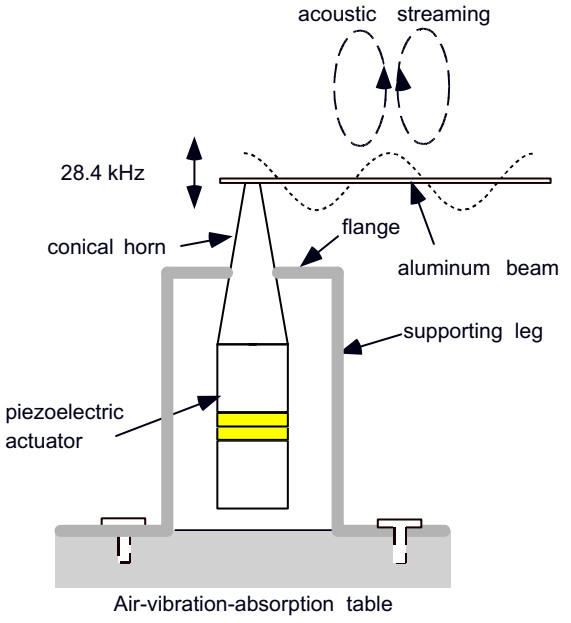

Fig. 1. Experimental setup.

where $A_L = A_v$ at the vibrating beam and $A_L = A_s$ at the stationary beam.

Note that in Eq. (4), any explicit dependence of acoustic streaming velocity on μ disappears although it originates from the viscosity. Acoustic streaming patterns in the gap depend on these two limiting velocities. Viscous losses associated with the wave propagation in the medium are proportional to the square of the excitation frequency (cf. [6]). CFD simulation in Section 4 indicates that at an ultrasonic excitation with a gap of 1 cm, the limiting velocity at the stationary beam becomes one tenth of the limiting velocity at the vibrating beam and that acoustic streaming is completely dominated by the latter. Therefore, with attenuation included, only a two circular airflow in the half-wavelength length is induced.

3. Experimental observations

3.1. Experimental setup

The experimental setup shown in Fig. 1 consists of a beam and modules that contain a piezoelectric actuator and a horn. The beam and horn are made of 6061-T6 aluminum because of the excellent acoustical characteristics of this material. The piezoelectric actuator is a bolted Langevin type transducer (BLT) designed to resonate at 28 kHz [16]. The conical horn is used to increase the amplitude of vibration supplied by the actuator. A conical geometry was selected because it not only gives a desired amplification ratio but can be easily machined. A mounting flange was included in the design of the horn and is located at the nodal lines where the velocity of vibration of the horn goes to zero. This allowed the mounting of the horn and BLT assembly onto a supporting base plate that was in turn bolted to the surface of an air-driven vibration absorption table. The small end of the horn was threaded to connect the beam with the horn using a machine screw. The dimension of the beam is determined such that one of the natural frequency of the beam is located in the vicinity of the resonant frequency of the actuator, thereby maximizing the displacement of the beam for a given power supply. The determined dimension is 10 mm wide, 1 mm thick and 128 mm long. Frequency spectrum analysis of the system shows that at an excitation frequency of 28.4 kHz, maximum vibration amplitude of the beam is achieved.

3.2. Flow visualization of acoustic streaming

To visualize acoustic streaming near the beam, the beam is excited at 28.4 kHz with a vibration amplitude of 10 μm [7]. Acetone is sprayed onto the vibrating beam. When Acetone comes in contact with the beam

it becomes small droplets and follows airflow pattern near the beam until it completely evaporates. A fiber optic lamp locally illuminates the region near the vibrating beam. Light is reflected from only Acetone droplets and the beam, making ambient air appear black. The whole process is videotaped using a camcorder. Fig. 2 shows a snap shot of the process. Unique features of acoustic streaming are observed. First, air rises above the anti-nodes and descends toward the nodes. Since vibration amplitude is not uniform along the length of the beam, the maximum distance to which Acetone droplets rise above the anti-nodes are not uniform either. Second, there exist two distinctive circular airflow within half wavelength that is 1 cm for this case. Clearer acoustic streaming is observed with bigger vibration amplitude.

3.3. Apparent acoustic streaming in the separation gap

Primary application of acoustic streaming considered in this study would be convective heat transfer augmentation. To this end, it is possible to contemplate that a heated object is placed over a vibrating beam near which acoustic streaming is induced. Then, the temperature of the heated object is decreased due to forced convection caused by acoustic streaming. Therefore, for heat transfer application, it is more important to study how acoustic streaming pattern is to change when there is a stationary upper beam. Specifically, the acoustic streaming velocity is a primary interest because convective heat transfer is proportional to the acoustic streaming velocity.

An aluminum beam that is 1 cm wide, 2.5 cm thick, and 11 cm long is placed 1 cm over the vibrating beam. The same visualization process used for the case without an upper stationary beam is performed at the gaps ranging from 2 mm to 1 cm. It is observed that acoustic streaming in the gap is strong enough to blow most of Acetone droplets out of the gap, making it almost impossible to perform visual observation of acoustic streaming pattern. Therefore, CFD simulation presented in Section 4 is used to estimate acoustic streaming pattern and velocity in the gap.

3.4. Indirect measurement of acoustic streaming velocity

Indirect measurement of acoustic streaming velocity is performed by measuring rotational velocity of a cylinder-shaped Styrofoam that is levitated and rotates in the gap as shown in Fig. 3. When a high intensity sound wave propagates, it propagates with a strong directionality. In other words, it does not scatter but propagates like a laser beam for a short distance of travel. Upon encountering a boundary, the wave is reflected, resulting in a pressure standing wave due to the interaction with the incident wave [17]. At a gap of 8 mm, a half-wavelength resonant pressure standing wave is created at an excitation frequency of 28 kHz. The resulting pressure standing wave is strong enough to levitate small objects. Objects in the gap are levitated above the velocity anti-nodes and stay at the midpoint of the gap where pressure is zero. Also, acoustic streaming causes objects to spin with a high rotational velocity. Theoretically, there exist two acoustic streaming patterns symmetrical with respect to the anti-nodes in every half-wavelength interval along the length of the beam. Due to the symmetry of acoustic streaming patterns, levitated objects should stand still above the anti-nodes. But induced acoustic streaming patterns are not perfectly symmetrical, causing the levitated objects to rotate owing to nonuniform thickness of the beam and the gap. Moreover, the width effect of the beam renders acoustic streaming pattern three-dimensional. In other words, twist and curl of circular airflow toward the width of the beam is observed. As a result, the axes of rotation for spinning objects are

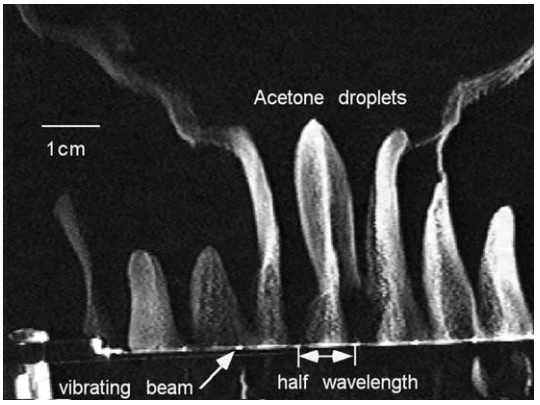

Fig. 2. Flow visualization of acoustic streaming over a ultrasonically vibrating surface.

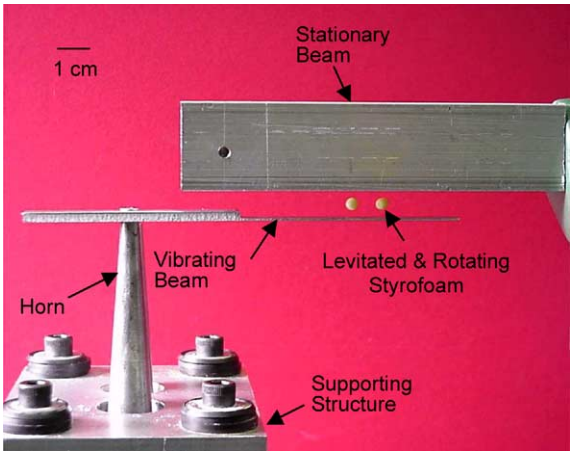

Fig. 3. Indirect measurement of streaming velocity using levitated objects.

not identical. The cylinder-shaped Styrofoam has a diameter of 2.8 mm and a length of 3 mm. The measured rotational velocity using a strobe light is approximately 2400 revolution per minute with a vibration amplitude of 10 μm, which correlates to a linear velocity of 0.35 m/s.

3.5. Convective heat transfer augmentation

To measure the enhancement of convective heat transfer due to acoustic streaming, a heat source containing an aluminum plate, a resistor, and a thermocouple is made. A detailed schematic drawing of the plate is shown in Fig. 4. The bottom of the plate is made of aluminum. The top is made of Plexiglas that contains a 600 Ω resistor and a thermocouple. The resistor is connected to a variable voltage power supply and serves as a heater. Temperature is measured on the aluminum surface which is bonded with resistant heater with Epoxy.

With the 600 Ω resistor, the temperature of the plate can be increased to 98 °C. During the experiment, the room temperature was kept at 20 °C. The heat source is placed 1.5 mm above the vibrating beam. As the temperature of heat source reaches a steady state value of 98 °C with a power supply of 3.4 W, acoustic streaming is generated by vibrating the beam at 28.4 kHz with a vibration amplitude of 10 μm. Then, the temperature changes of the plate are measured using the thermocouple. Due to the inherent noises in the voltage signal from the thermocouple, the signal is filtered through a low pass filter and sampled at 20 Hz using a data acquisition board. A temperature drop of 30 °C is achieved in 4 min and maintained as shown in Fig. 5. As the vibration amplitude is further increased to 25 μm a temperature drop of 40 °C is achieved that is the maximum temperature drop obtained with the current experimental setup.

When acoustic streaming is induced in the gap there are two possible major heat flow paths. The first one is convective heat transfer to ambient air in the direction parallel to the hear source marked as heat flow path 1 in Fig. 6. In this path, the heat from the heat source is taken away by airflow near the heat source and transferred to ambient air without making significant heat transfer to the vibrating beam. The second path is convective heat transfer through the vibrating beam marked as heat flow path 2. Due to the circular nature of acoustic streaming pattern, in the second path the heat from the heat source is delivered to the vibrating beam and dissipated to ambient air.

In order to measure the heat transfer in path 1, the space between the heat source and the vibrating beam is enclosed along the perimeter of heat source using a masking tape, thereby allowing heat to flow only in path 2. However, since the beam is vibrating at an ultrasonic frequency, it is impossible to achieve complete enclosure. As shown in Fig. 7, when enclosed achieved temperature drop is 10 °C less than when it is not enclosed, which is 33% decrease in the temperature drop. In addition, to gauge the heat flow in the path 2, changes in the temperature of the vibrating beam are measured as shown Fig. 8. When the heat source is heated to 98 °C the temperature of the lower beam is increased to 36 °C as a result of conduction through air. When induced, acoustic streaming causes the temperature of the vibrating beam to drop to 26 °C in 2 min, which is 6 °C is higher than the room temperature. It is also observed that the obtained temperature drop changes with the gap.

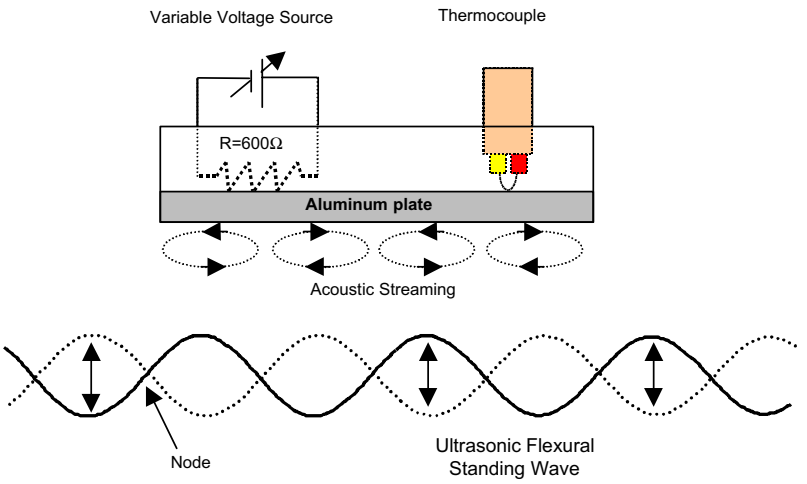

Fig. 4. Experimental setup for measuring heat transfer augmentation.

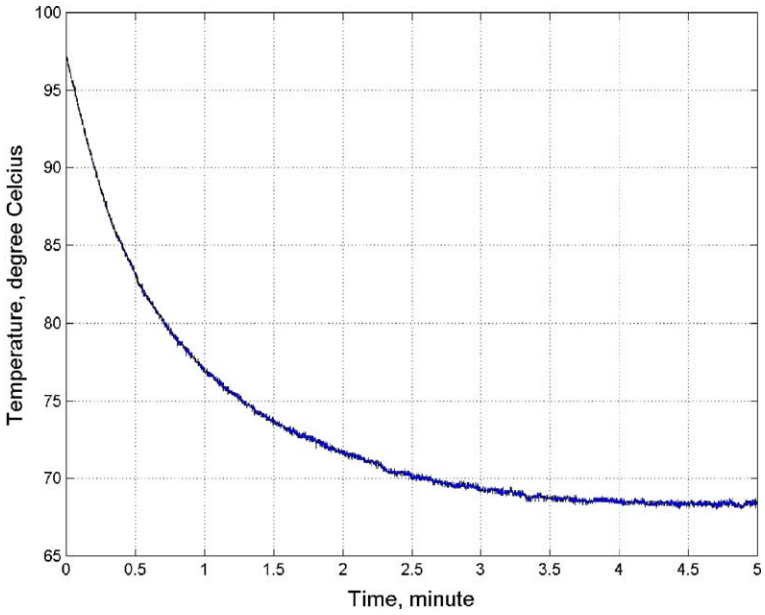

Fig. 5. Temperature drop of the heat source.

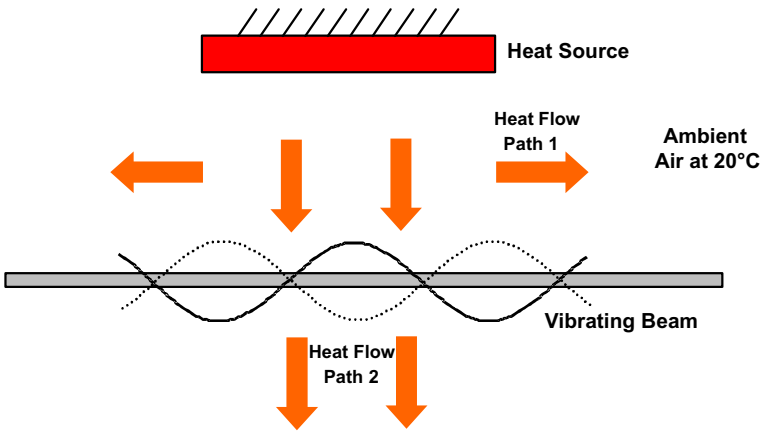

Fig. 6. Simplified diagram of the heat flow paths.

4. Analytic heat transfer and numerical simulations

4.1. Governing equations

Fig. 9 exhibits schematically the two-dimensional channel model of the ultrasonic flexural standing waves (UFSW) system. The model consists of the lower, very thin vibrating plate (UFSW) and the upper rigid three-layer plate with a controlled volumetric heat source ($\dot{q} = 3.2\,\mathrm{W}$) as shown in Fig. 10. The vertical displacement of the lower vibrating surface is given by

$$y = A(t)\cos(2\pi x/\lambda) \tag{5}$$

where $A(t)$ is the wave amplitude, $A(t) = A_0 \sin(\omega t)$. The mathematical models described below are 1-D and 2-D simplifications of the actual experimental apparatus discussed previously.

The Reynolds number based on the representative conditions, i.e., the thickness of the gap is 2 mm, A_0 is 25 μm, λ is 1 cm, and f is 28 kHz, is less than 1800, which is in the region of laminar flow. The air velocity in the gap is less than Mach 0.3 so that the incompressible fluid assumption can be applied. The governing equations for incompressible transient laminar Newtonian fluid flow are continuity equation as follows:

$$\nabla \cdot \vec{\mathbf{v}} = 0 \tag{6}$$

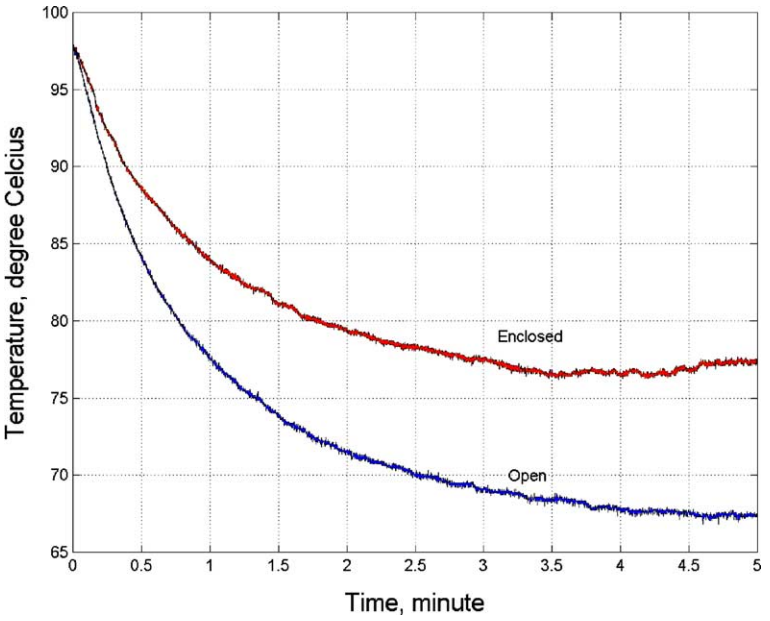

Fig. 7. Effect of enclosing the heat source for temperature drop.

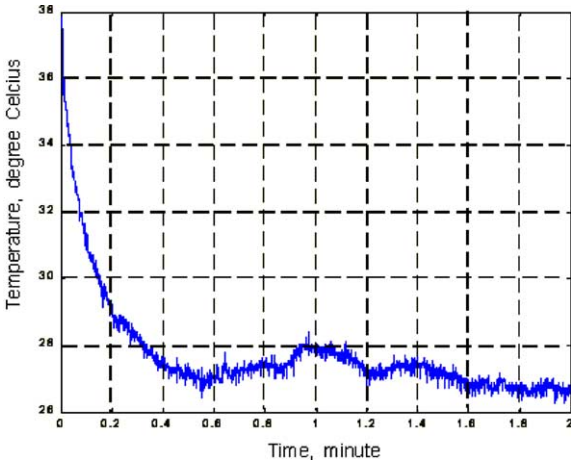

Fig. 8. Temperature drop of the vibrating surface.

and linear momentum equation as;

$$\frac{\partial \vec{\mathbf{v}}}{\partial t} + (\vec{\mathbf{v}} \cdot \nabla)\,\vec{\mathbf{v}} = \frac{1}{\rho}(-\nabla p + \mu \nabla^2 \vec{\mathbf{v}}) \tag{7}$$

The velocity $\vec{\mathbf{v}}$, which contains harmonic terms and a "dc" term, is calculated from Eqs. (6) and (7) and the acoustic streaming velocity ($\vec{v}_{\mathrm{a},i}$, $i = 1,2,3$) is obtained by averaging $\vec{\mathbf{v}}$ over a period as follows:

$$\vec{v}_{\mathrm{a},i} = \frac{1}{T_{\mathrm{a}}} \int_0^{T_{\mathrm{a}}} v_i \mathrm{d}t \quad i = 1,2,3 \tag{8}$$

where T_{a} is the period. Using the acoustic streaming velocity obtained from Eq. (8), the convective heat transfer equation can be solved numerically [18], which is given by:

$$\rho C_{\mathrm{p}} \frac{\mathrm{D}T}{\mathrm{D}t} = k\nabla^2 T + \mu \left(\frac{\partial \vec{v}_{\mathrm{a},i}}{\partial x_j} + \frac{\partial \vec{v}_{\mathrm{a},j}}{\partial x_i} \right) \frac{\partial \vec{v}_{\mathrm{a},i}}{\partial x_j} \tag{9}$$

where i and j = 1,2,3. The lumped energy approach is applied to the transient 1-D system shown in Fig. 11 with heat generation in the plate and heat loss through the surfaces, i.e.,

$$\frac{\mathrm{d}E}{\mathrm{d}t} = -2Aq_n \tag{10}$$

where A denotes the surface area of one side of the plate and q_n is the heat flux at the surface. The left hand side of Eq. (10) can be expressed as

$$\frac{\mathrm{d}E}{\mathrm{d}t} = \rho(2AL)C_{\mathrm{p}} \frac{\mathrm{d}T}{\mathrm{d}t} - (2AL)\dot{q}''' \tag{11}$$

where L is the plate thickness, C_{p} is the specific heat of the plate material, T is the lumped temperature of the plate, and $\dot{q}'''$ is the constant heat generation rate in the plate. Thus, the energy balance for this system can be stated as

$$\rho L C_{\mathrm{p}} \frac{\mathrm{d}T}{\mathrm{d}t} = -q_n + L\dot{q}''' \tag{12}$$

with the initial and boundary conditions given by

$$T(0) = T_i \quad \text{and} \quad q_n = h(T - T_\infty) \tag{13a, b}$$

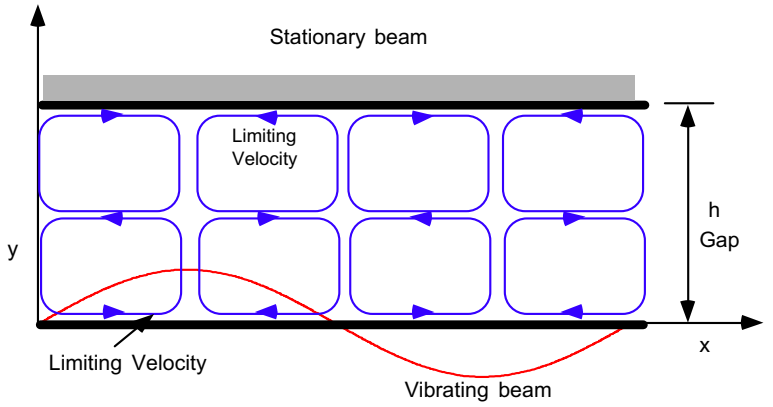

Fig. 9. Theoretically estimated acoustic streaming pattern without attenuation.

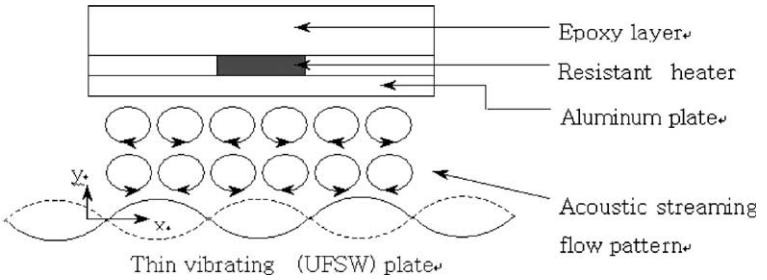

Fig. 10. Schematic diagram of the system.

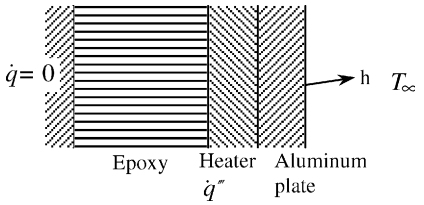

Fig. 11. 1-D analytical heat transfer model.

where T_∞ is the ambient air temperature outside of the thermal boundary layer.

Substituting Eq. (13b) into Eq. (12) gives

$$\rho L C_p \frac{dT}{dt} = -h(T - T_\infty) + L\dot{q}''' \tag{14}$$

subject to Eq. (13a). The answer is given by

$$T = \left(T_\infty + \frac{\dot{q}'''L}{h}\right) + \left(T_i - T_\infty - \frac{\dot{q}'''L}{h}\right)\exp\left(-\frac{ht}{\rho C_p L}\right) \tag{15}$$

where T_∞, $\dot{q}'''$, and T_i are known and h can be estimated for infinite rectangular tubes. The convective heat transfer coefficient h is calculated based on the empirical relationship (cf. [19]). Nusselt number (Nu_m) from Kay and Crawford [19] is about 9.9 for the rectangular tube case. The averaged convective heat transfer coefficient can be calculated from the definition of the Nusselt number and is about 141.0 W/m^{2}K for the base case. (cf. [19]).

4.2. Analytical and numerical results

Fig. 12 shows the time-evolution of vortices in the gap due to acoustic streaming. At time $t = 0.0$, no air flow exists in the gap, and then the lower wall starts to vibrate with the frequency $f = 28.4$ kHz, vibration amplitude $A_{max} = 20\,\mu$m and wavelength $\lambda = 2.0$ cm in a 2 mm gap between two plates. Four vortices over a single wavelength emerge near the lower vibrating plate (cf. Fig. 12a). They appear in-between nodal points and anti-nodal points of the vibrating wave with two of them in the center moving closer (cf. Fig. 12a-l). The air flows upward at anti-nodal points and downward at nodal points, which is similar to the experimental visualization shown in Fig. 1. After 610 pulses a steady streaming flow field is achieved (cf. Fig. 12f-l).

Fig. 13 represents the acoustic streaming velocity tangent and normal to the plate along a fictitious vertical line passing through a vortex center. The tangential

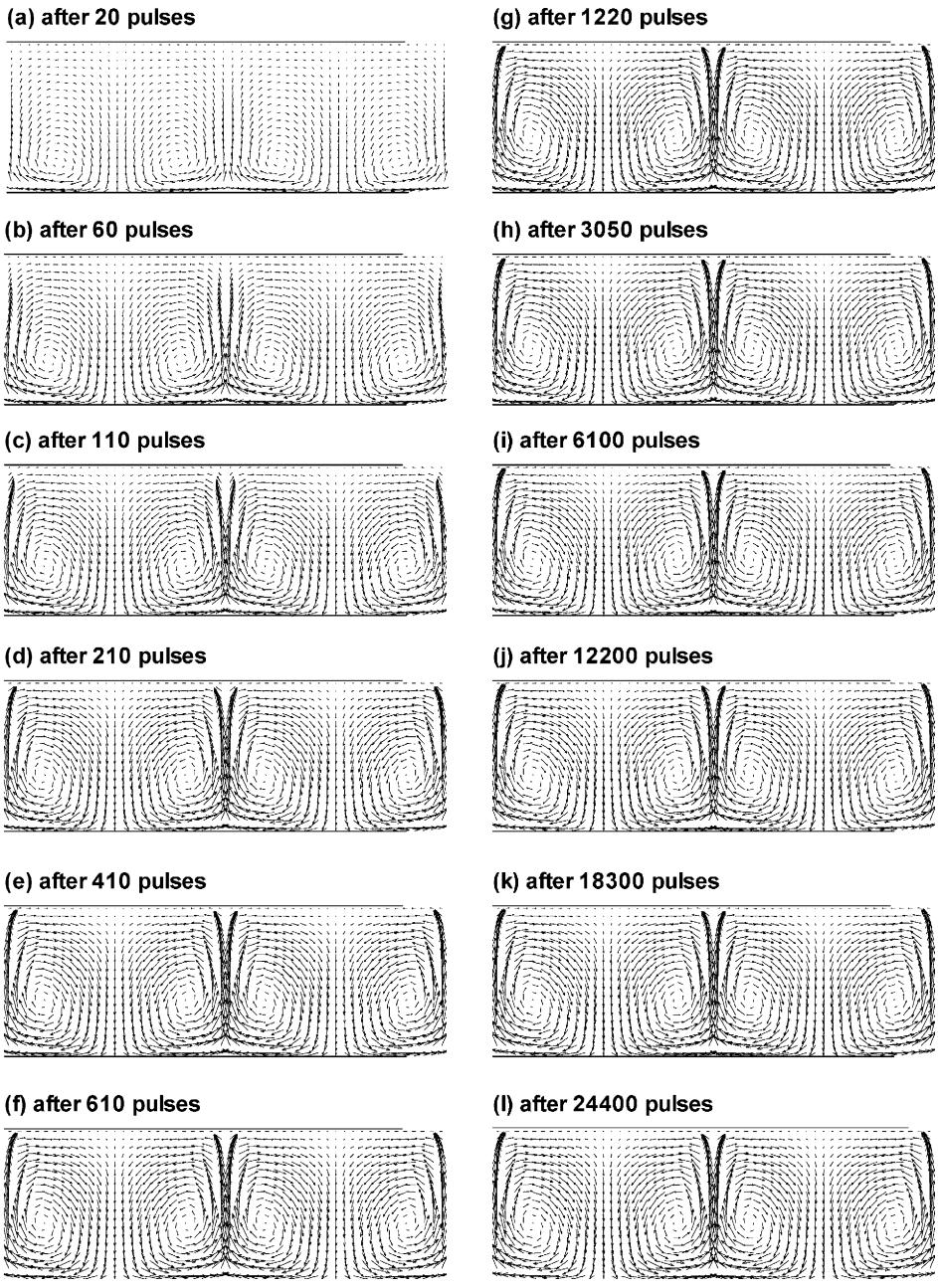

Fig. 12. Time evolution of the streaming velocity field in the gap.

and normal velocities are zero at the vortex center (about $y = 0.072$ mm). The tangential velocity reaches 70 cm/s near the lower vibrating plate and 30 cm/s near the upper plate. The normal velocity is significant only near the nodal and anti-nodal points, and near zero along the vertical line through the vortex center as shown in the flow field of the converged solution in Fig. 12l.

To observe the effect of changing excitation frequency, vibration amplitude, and gap on the streaming velocity and patterns, simulations were performed with the conditions detailed in Table 1. To maintain the first order velocity at a constant value, the vibration amplitude decreases as the excitation frequency increases. It is observed that the vortical flow patterns are not effected by changing simulation conditions but

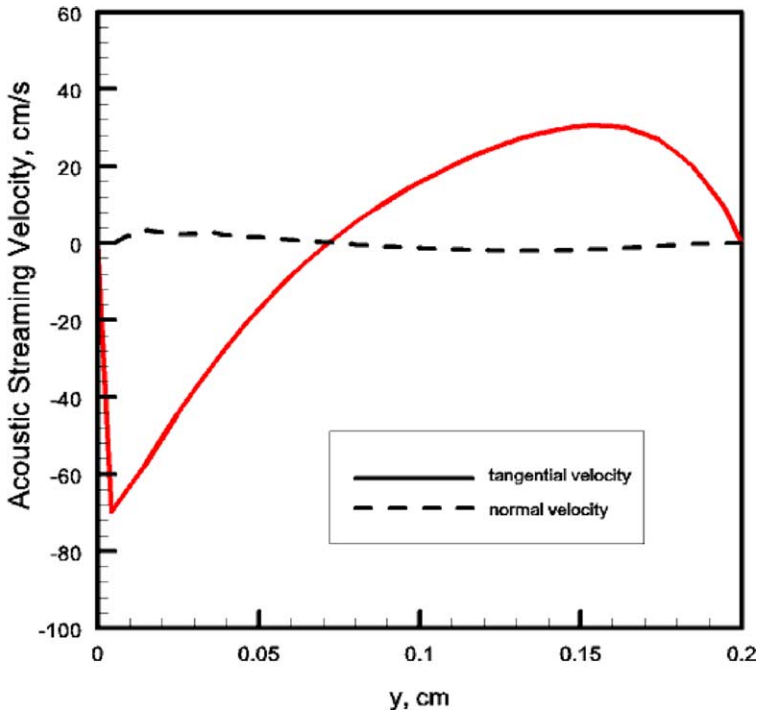

Fig. 13. Streaming velocity distribution along the cross-section through the vortex center.

the magnitude of the acoustic streaming velocity is strongly effected. Therefore, for the following analyses only the variations of the magnitude of streaming velocity along a vortex center are compared and discussed except for the case of open ends in Section 4.2.3.

4.2.1. Effect of vibration frequency

Fig. 14a shows the maximum acoustic streaming velocity at 50 μm above both lower and upper plates in the 2 mm gap at an frequency of 6, 12, 18, 28.4 and 50 kHz. It is observed that the maximum streaming velocities near the lower UFSW plate is about twice those of the upper plate. The maximum streaming velocities at 28.4 kHz near the lower and upper plates are 66.2 cm/s and 30.6 cm/s, respectively. The acoustic streaming motions near the lower plate are directly influenced by the motion of the lower vibrating plate while streaming motions near the upper plate are induced by the streaming flow near the lower plate. In the process of inducing streaming motions near the upper plate, airflow is diminished. As a result, the maximum streaming velocities are observed near the lower plate. According to Nyborg's theory in Eq. (4), if the first-order velocity is held constant, the acoustic streaming velocity also should be constant. However, results present that the maximum streaming velocity decreases with excitation frequency.

Table 1
System properties for CFD simulations (cf. Fig. 14a)

Frequency (kHz)	Vibration amplitude (μm)	First order velocity (m/s)	Wavelength (mm)
6.0	93.0	3.5	48.0
12.0	47.0	3.5	34.0
18.0	31.0	3.5	28.0
28.4	20.0	3.5	20.0
50.0	11.0	3.5	17.0

4.2.2. Effect of vibration amplitude and separation gap

Fig. 14b shows the maximum streaming velocities near the plates for a vibration amplitude of 5, 10, 15, 20, 25, 30 and 40 μm with a gap of 2 mm at an excitation frequency of 28.4 kHz. The wavelength is 20 mm. The maximum streaming velocity increases as the vibration amplitude increases because the first-order velocity increases. The maximum first-order velocity near the lower vibrating plate can be computed with the excitation frequency and the vibration amplitude of the plate. The maximum first-order velocities for the base case (vibration amplitude 20 μm) and the cases of 5 and 40 μm vibration amplitudes are approximately 3.5 m/s, 0.9 m/s and 7.0 m/s, respectively. For the vibration amplitudes greater than 15 μm, the maximum streaming velocities increases linearly with the vibration amplitude. For a vibration amplitude of 25 μm, the maximum streaming

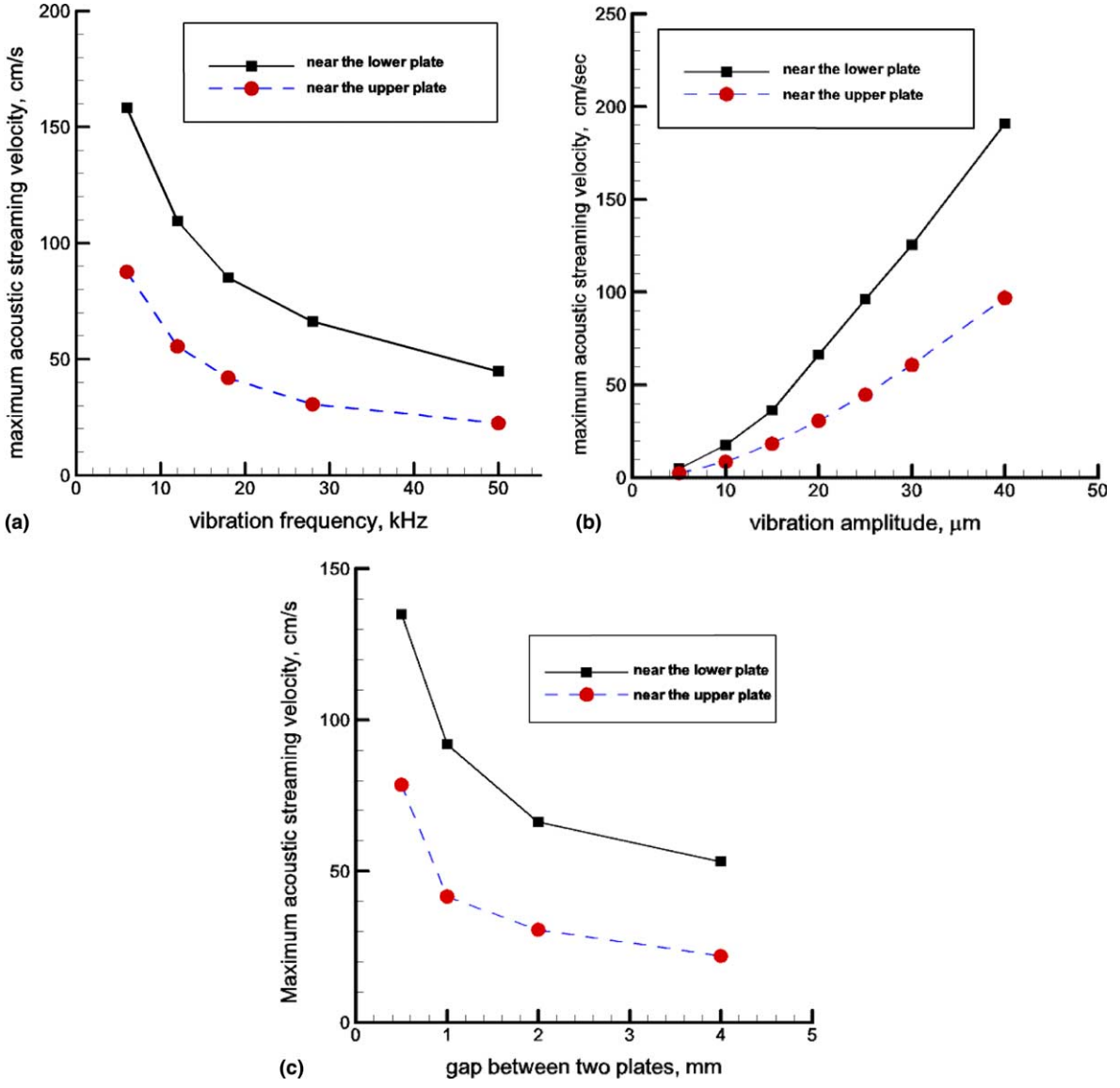

Fig. 14. (a) Maximum acoustic streaming velocity at 50 μm above both lower and upper plates for constant first-order velocity cases. (b) Maximum acoustic streaming velocity at 50 μm above both lower and upper plates for different vibration amplitude. (c) Maximum acoustic streaming velocity at 50 μm above both lower and upper plates for gap sizes.

velocities near the lower and upper plates reach 100 cm/s and 45 cm/s, respectively. For a vibration amplitude of 40 μm, the maximum streaming velocities near the lower and upper plates are 190 cm/s and 97 cm/s, respectively.

Fig. 14c represents the maximum acoustic streaming velocities for different gap sizes. The maximum streaming velocity decreases as the gap between the two plates increases. The rate at which maximum streaming velocity decreases for gaps under 1 mm is greater than that for gaps over 1 mm.

4.2.3. Effect of surface end openings

Fig. 15 shows the streaming velocity fields for the 2 mm gap case considering the entire system, i.e., a one-and-a-half- wavelength long vibrating plate (3 cm) and a one-wavelength long rigid upper plate (2 cm) to observe the effect of an open-ended channel. Vortical flow and flow entrainment are observed near the ends of the upper plate. The vortex centers in the channel are located at the location, $x = 0.3$ and 0.65 cm. Due to air entrainment, the flow field near the end is disturbed and a small vortex is formed (cf. enlarged Fig.

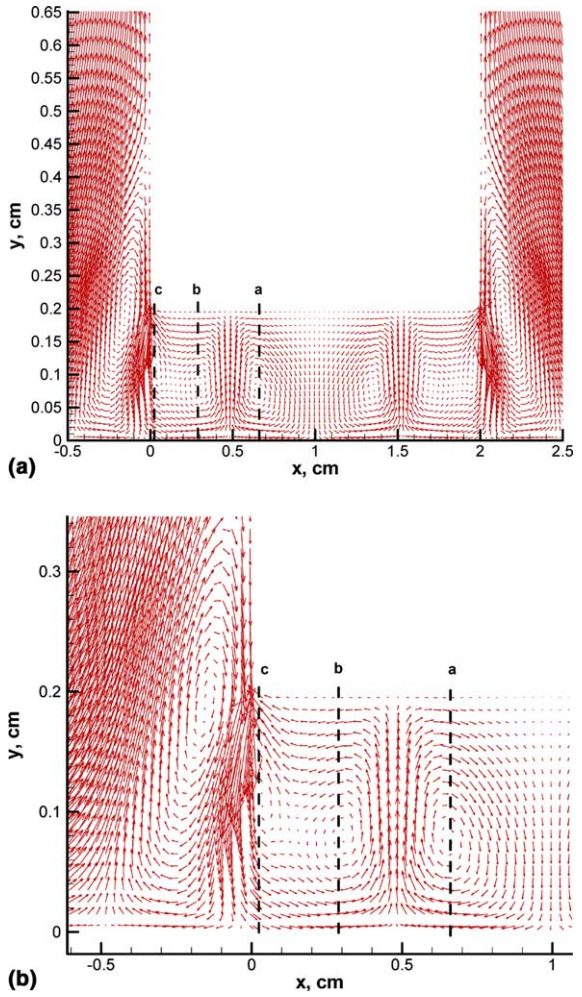

Fig. 15. (a) Streaming velocity fields for the 2 mm gap case considering the entire system and (b) enlarged view of the streaming velocity fields near the end.

15b). The tangential and normal velocity components along path a, b, and c are given in Fig. 16. For the inner vortex (solid and dotted lines in Fig. 16), the tangential velocity denoted by u reaches 120 cm/s near the lower plate, 60 cm/s above the vortical center, and 25 cm/s near the upper plate. For the outer vortex (dashed and long dashed lines in Fig. 16), the tangential velocity reach 60 cm/s near the lower plate and 100 cm/s near the upper plate. Clearly, the velocities near the two plates are greater than those for the same gap size without plate end openings (cf. Fig. 14c). The velocity near the upper plate with the flow reentrainment reaches up to 115 cm /s and is almost twice the 2 mm gap case without flow entrainment. Thus, flow entrainment enhances the flow speed and changes the flow pattern, resulting in enhanced cooling capability.

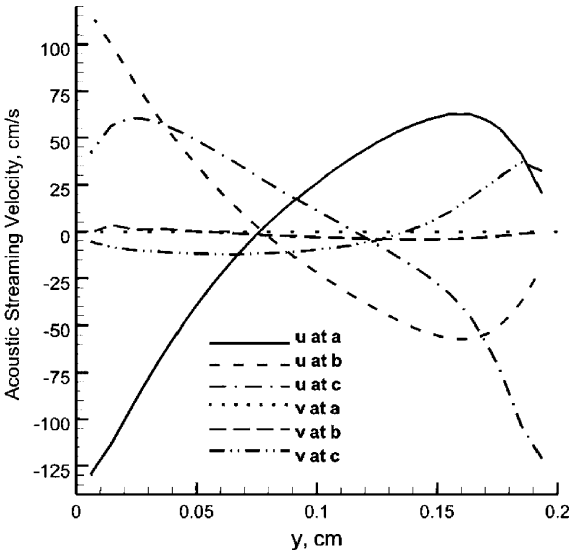

Fig. 16. Streaming velocity distribution along the cross-sections through the vortex centers for the entire system.

Fig. 17 shows the magnitude of the acoustic streaming velocity in the gap from a three-dimensional perspective. A maximum streaming velocity occurs right at the openings of the gap near the upper plate, which enhances the mixing of flow between inside and outside the gap. The streaming velocities near the lower plate are generally greater than those near the upper plate except the maximum streaming velocity occurring at the openings.

4.2.4. Heat transfer results

Fig. 18 represents the transient temperature profiles for the upper plate obtained with the analytic solution (Eq. (15)), computational convective heat transfer simulation using Eq. (9) as well as experimental measurements. The temperature distributions from the computational convective heat transfer simulation will be discussed below. The initial temperature of the plate, T_i, and the air temperature, T_∞, were given as 96.8 °C and 20.0 °C, respectively, and the calculated temperature at time $t = 300$ sec. is compared to the measured temperature ($T_{measure} = 68.0$ °C). From the analytic solution, the convective heat transfer coefficient, h, for this system with a 3.2 W heat generation rate is calculated as 152.6 W/m^{2}K. In comparison, using thermal-entry-length Nusselt number value with the maximum acoustic streaming velocity for the base case, the heat transfer coefficient is about 141.0 W/m^{2}K, which is within acceptable bounds (cf. Fig. 17 and [19]). With the constant convective heat transfer coefficient value, $h = 152.6$ W/m^{2}K, the temperature profile of the upper aluminum plate is obtained using Eq. (15). For this analytical calculation, it is assumed that there is no temper-

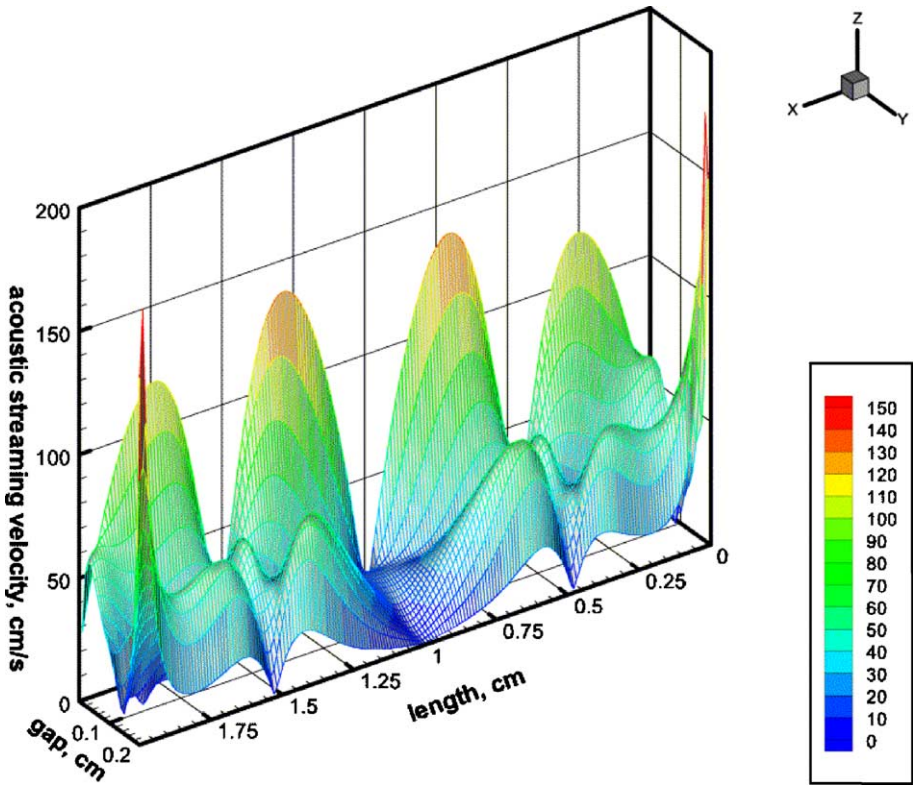

Fig. 17. 3-D streaming velocity contours inside the gap between two plates.

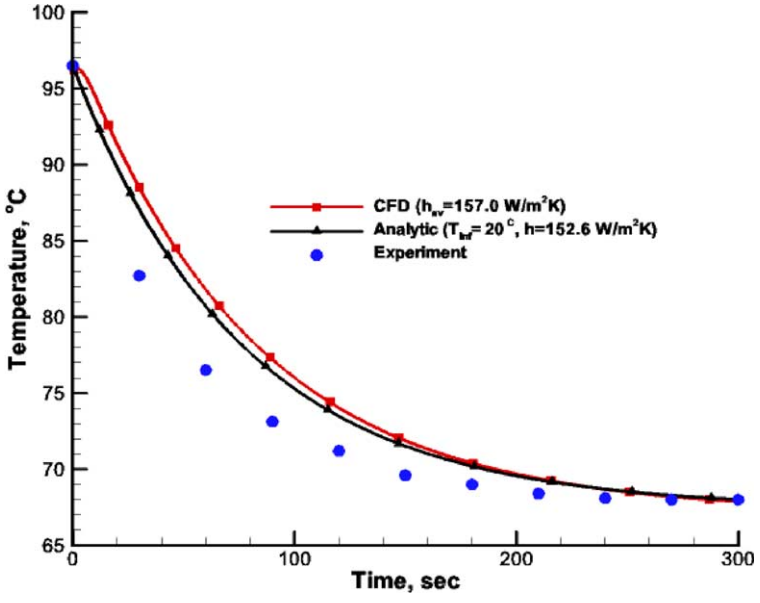

Fig. 18. Transient temperature drop for the upper plate (analytic solution, computational simulation, experimental measurements).

ature gradient in the thin aluminum plate, the temperature and the thermal properties are for the thermal insulator or heat generator (material: epoxy), the thickness of the plate is assumed 5 mm, which is the total thickness

of the upper plate assembly, and the back side of the upper plate assembly is insulated to maintain the direction of the heat flux toward the surface.

Using the two-dimensional time-dependent convective heat transfer Eq. (9), the time-dependent temperature contour fields in the 2.0 mm gap with plates are shown in Fig. 19. The upper plate consists of three layers–a 1 mm thick aluminum plate, a 1 mm thick heat generator ($\dot{q} = 3.2$ W) and a 3 mm thick thermal insulator (cf. Fig. 10). It is assumed that the thermal properties for the conducting solids and air are constant, the initial temperatures for the upper plate and the air in the gap are 369.15 K, and the ambient air temperature is 293.15 K. The total convective heat transfer coefficient at the surfaces of the upper plate for the computational convective heat transfer simulation is similar to the calculated value using Eq. (9), which is 152.6 W/m^{2}K. From several trials, the convective heat transfer coefficient at the surface between the upper aluminum plate and the air is determined to be 50 to 60 W/m^{2}K. The flow fields are simulated based on a two-dimensional geometry; however, the experimental flow field exhibited a strong three-dimensional effect. The conduction heat transfer through the supporting materials cannot be ignored. Thus, it is assumed that the convective heat transfer coefficient from the upper surface of the thermal insulator is about 100 W/m^{2}K to accommodate all extra heat losses. This implies that three-dimensional convective heat transfer effects, with flow entrainment from the ambient, play a very important role in the thermal cooling mechanism of the actual system. The quasi-steady acoustic streaming velocity values (cf. Fig. 15) are applied as an initial condition and the flow field does not change with time. At $t = 20$ sec., the temperatures in the upper and lower plates are about 360.0 K and 293.0 K, respectively (cf. Fig. 19a). The temperature in the middle, affected by the down-flow from the heated upper plate, is higher than the temperature in the vortical center and the temperature for the upward moving air is lowest in the gap, which is about 300.0 K. After 100 s (cf. Fig. 19b), the temperature in the upper plate is about 340 K. There is no temperature gradient in the upper and lower aluminum plates, which have high thermal conductivities. Due to the flow reentrainment and vortical flow field near the side openings, temperature gradients can be observed. A similar temperature contour field can be found at time $t = 300$ s, as shown in Fig. 19c.

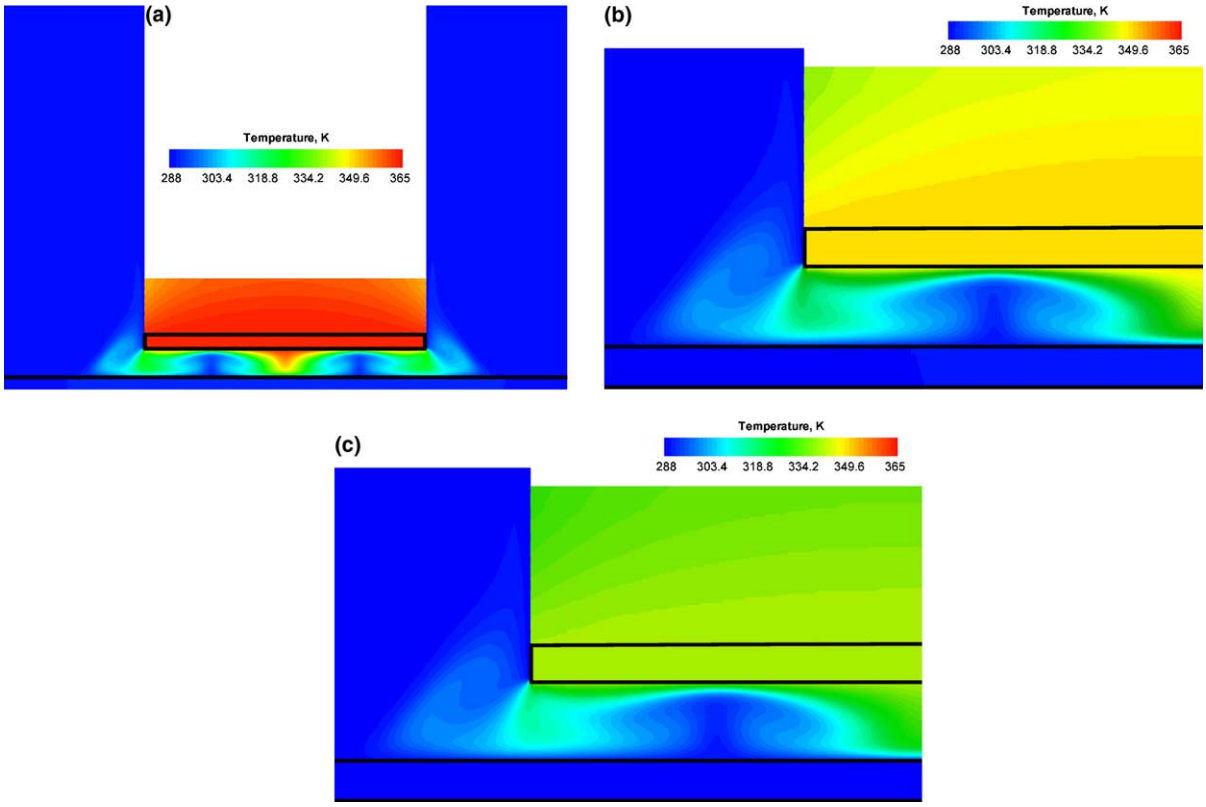

Fig. 19. Time-dependent temperature contour fields in the 2.0 mm gap with the entire system. Temperature field (a) At $t = 20$ s; (b) at $t = 100$ s; and (c) at $t = 300$ s.

Using the effective convective heat transfer coefficient in the computational heat transfer simulations, the transient temperature profile of the upper aluminum plate is similar to that from experimental measurements as well as the analytic solution using Eq. (15) (cf. Fig. 18). The convective heat transfer coefficient for the lower surface of the upper plate assembly form the CFD is calculated as 57.0 W/m^2K. Thus, the total convective heat transfer coefficient for the upper plate assembly is 157.0 W/m^2K, which is similar to the value used for analytic solution.

5. Conclusions

An investigation of acoustic streaming induced by ultrasonic flexural vibrations is presented. The investigation includes acoustic streaming pattern, velocity, and associated heat transfer characteristics. By virtue of acoustic streaming, a notable temperature drop of 40 °C was obtained in 4 min and maintained. Tests identifying major heat flow paths indicated that gaps and the vibrating beam serve as major heat flow paths.

CFD simulations were conducted to observe acoustic streaming patterns and velocities in the gap. Simulation results were validated by performing heat transfer analysis based on a lump-energy method. Simulation predicted that two symmetric vortices within half wavelength, rise of air at anti-nodes, and descent at nodes as Nyborg's theory predicts. The presence of the upper plate has no effect on the acoustic streaming patterns. However, when an upper plate shorter than the vibrating plate is used, a drastic increase in streaming velocity occurs at the edges of the upper plate due to entrainment of air, which also alters streaming pattern in the vicinity of the open end. The results of CFD simulations indicated the vortical flows induced by a UFSW can be reproduced. The CFD results are experimentally validated, qualitatively through flow pattern comparisons and quantitatively by the transient temperature drop comparison.

From the computational heat transfer simulations, it is very important to include a reasonable heat transfer coefficient for the lower plate, which is long and of high conductivity material. Using appropriate boundary conditions, the time-dependent temperature contour fields are obtained and compared to the measured temperature drop for the heated surface. The heat loss from actual three-dimensional flow fields and subsequent heat transfer effects is much larger than the heat loss through the lower surface of the upper plate assembly. Hence, it is recommended that three-dimensional flow field simulations as well as convective heat transfer simulations should be conducted to obtain more realistic solutions without resorting to prescribed "effective" heat transfer coefficients.

The theoretical calculations based on sonically induced acoustic streaming may not be extended to ultrasonically induced acoustic streaming calculations. The acoustic streaming flow pattern from theoretical calculations without viscous dissipation effects do not match to the flow patterns from experimental observations or CFD simulations. Flow reentrainment at the channel ends enhances convective heat transfer and can not be captured with theoretical calculations. As shown in the visualization experiment of acoustic streaming over an ultrasonically vibrating beam, an imperfect experimental set-up causes three-dimensional effect including curl and swirl of airflow to occur. Therefore, for more in-depth study on streaming patterns and associated heat transfer capability, three-dimensional analysis is needed.

References

[1] C.P. Lee, T.G. Wang, Outer acoustic streaming, J. Acoust Soc. Am. 88 (5) (1990) 2367–2375.
[2] W.L. Nyborg, Acoustic streaming near a boundary, J. Acoust. Soc. Am. 30 (4) (1958) 329–339.
[3] M. Faraday, Phil.Trans. 121 (1831) 229.
[4] L. Rayleigh, Theory of Sound, Dover Publication, New York, 1945.
[5] H. Schlicting, Boundary Layer Theory, McGrow-Hill Book Company Inc., New York, 1955.
[6] J. Lighthill, Acoustic streaming, J. Sound Vib. 61 (3) (1978) 391–418.
[7] F.J. Jackson, W.L. Nyborg, Sonically-induced microstreaming near a plane boundary. II. Acoustic streaming field, J. Acoust. Soc. Am. 32 (11) (1960) 1387–1396.
[8] N.T. Nguyen, R.M. White, Design and optimization of an ultrasonic flexural wave micropump using numerical simulation, Sensor. Actuat. 77 (1999) 229–236.
[9] R.K Gould, Heat transfer across a solid–liquid interface in the presence of acoustic streaming, J. Acoust. Soc. Am. 40 (1) (1966) 219–225.
[10] A. Gopinath, F. Mills, Convective heat transfer from a sphere due to acoustic streaming, J. Heat Transfer 115 (1993) 332–341.
[11] A. Gopinath, F. Mills, Convective heat transfer due to acoustic streaming across the ends of kundt tube, J. Heat Transfer 116 (1994) 47–53.
[12] V. Uhlenwinkel, R. Meng, K. Bauckhage, P. Schreckenber, O. Andersen, Heat transfer to cylindrical bodies and small particles in an ultrasonic standing-wave fields of melt atomizer, in: Multiphase-flow and Heat Transfer in Materials Processing ASME, FED-vol. 201/HTD-vol, 297, 1994, pp. 19–24.
[13] P. Vainshtein, M. Fichman, C. Cutfinger, Acoustic enhancement of heat transfer between two parallel plates, Int. J. Heat Mass Transfer 38 (10) (1995) 1893–1899.
[14] Z.D. Chen, M.P. Taylor, J.J.J. Chen, Heat transfer on a surface affected by an air/water interface undergoing wave motion, Miner. Met. Mater. Soc. (1998) 429–435.

[15] J.M. Andres, U. Ingard, Acoustic streaming at high reynolds numbers, J. Acoust. Soc. Am. 25 (5) (1953) 928–937.
[16] T. Sashida, An Introduction to Ultrasonic Motors, Clarendon Press, Oxford, 1993.
[17] F.S. Sherman, Viscous Flow, McGraw-Hill Book Company, Inc., New York, 1990.
[18] S.J. Yang, Numerical study of heat transfer enhancement in a channel flow using an oscillating vortex generator, Heat Mass Transfer 39 (2003) 257–265.
[19] W.M. Kays, M.E. Crawford, Convective Heat and Mass Transfer, McGraw-Hill, New York, 1993.